Twist-Enhanced Thermoelectric Effect in $Cr(pyz)_4$-Based Heterojunction via Tuning Spin Quantum Interference

Li-Hua Luo(罗丽华)[1], Shi-Hua Tan(谭仕华)[1], Xiao-Fang Peng(彭小芳)[1*], and Meng-Qiu Long(龙孟秋)[2*]

[1]*Hunan Province Key Laboratory of Materials Surface or Interface Science and Technology, Central South University of Forestry and Technology, Changsha 410004, China*
[2]*School of Physics and Electronics, Central South University, Changsha 410083, China*

(Received 10 February 2026; accepted manuscript online 8 April 2026)

Quantum interference, which usually occurs in some symmetric molecular rings, has great potential for the realization of high-performance thermoelectric conversion. Twisting molecular rings in molecular junctions provides a unique approach to tuning quantum interference, thus enabling the development of high-performance molecular thermoelectric devices. In this work, using density functional theory combined with the non-equilibrium Green's function method, we investigate the spin-dependent thermoelectric properties of a $Cr(pyz)_4$ (pyz = pyrazine) magnetic molecule sandwiched between two ferromagnetic zigzag graphene nanoribbon (ZGNR) electrodes. The results show that twisting between the pyrazine rings and graphene electrodes can significantly enhance the electronic conductance and the Seebeck coefficient. The main reason is that twisting can modulate quantum interference: it enhances the transmission of spin-up electrons via constructive spin interference, thus increasing the conductance; meanwhile, it induces sharp antiresonances for spin-down electrons via destructive spin interference, thus enhancing the Seebeck coefficient. In addition, twisting can also strengthen phonon scattering, leading to a lower phonon thermal conductance. Combining these factors, we find that the thermoelectric performance can be effectively regulated and greatly improved in twisted $Cr(pyz)_4$-based heterojunctions: the $Z_{sp}T$ exceeds 4 at 300 K and reaches 6 at 340 K.

DOI: 10.1088/0256-307X/43/5/050803 CSTR: 32039.14.0256-307X.43.5.050803

1. Introduction. Charge transport in highly symmetric molecular rings is dominated by quantum effects that can be modulated through the electron wavefunction.[1] These novel quantum effects, such as quantum interference (QI),[2,3] provide a promising strategy for the design of high-performance thermoelectric (TE) devices. In single-molecule junctions, electron waves propagate through discrete molecular orbitals and undergo constructive or destructive interference; QI in this process can be directly observed in transport spectra[4] and tuned by molecular-junction symmetry,[5,6] electrochemical gating,[7] nanoribbon length,[8] and doping.[9] Furthermore, in certain magnetic molecular configurations, distinct spin states correspond to unique interference patterns. In such magnetic molecular junctions, both destructive spin interference (DSI) and constructive spin interference (CSI) can be realized,[10] offering a unique pathway for the wide-ranging modulation of thermoelectric performance.[4,11]

TE materials, capable of directly converting heat into electricity and vice versa, have been known for nearly two centuries and have attracted extensive attention in recent years.[12–14] The efficiency of a thermoelectric device can be quantified by a dimensionless figure of merit $ZT = TGS^2/(K_e + K_{ph})$ (where T is temperature, G is electronic conductance, S is Seebeck coefficient, K_e is electronic thermal conductance, and K_{ph} is the lattice thermal conductance[15]). Conventional commercial TE materials[16–18] suffer from two critical bottlenecks: high toxicity and low thermoelectric conversion efficiency, which hinder their large-scale applications. Therefore, the exploration of high-performance TE materials has become a major challenge and research hotspot currently.[19] To date, extensive efforts have been devoted to this field. Many molecular thermoelectric devices assembled from single molecules, including porphyrin single-molecule junctions,[5] porphyrin dimer molecules,[20] adenine and porphine,[21] and DNA molecules,[22] have emerged as research hotspots in the thermoelectric community owing to their low K_{ph}, high Seebeck coefficient S, and thus high thermoelectric figure of merit ZT. Investigating the thermoelectric properties of molecular heterojunctions offers opportunities for designing novel quantum thermoelectric devices with superior thermoelectric performance.[9] In particular, in magnetic molecule-based heterojunctions, the thermoelectric performance can be further improved by employing spin as an additional degree of freedom.[23] Excellent thermoelectric performance has also been reported in various magnetic molecular structures, such as twisted triangulene π-dimer junctions,[24] metallocene dimer-based molecular junctions,[25] and metallo-organic magnetic molecules.[26]

*Corresponding authors. Email: xiaofangpeng@csuft.edu.cn; mqlong@csu.edu.cn
© 2026 Chinese Physical Society and IOP Publishing Ltd. All rights, including for text and data mining, AI training, and similar technologies, are reserved.

Benzene, a symmetric six-membered molecular ring, can be constructed into novel molecular junctions. QI effects exist in these junctions,[27] and it is promising to achieve enhanced thermoelectric properties by exploiting such QI effects.[28–30] In particular, by introducing nitrogen atoms into the benzene ring, we obtain another symmetric six-membered molecular ring, pyrazine, which is widely used as a building block for organic molecules.[31] A two-dimensional (2D) metal-organic magnet $Cr(pyz)_2$ (pyz = pyrazine), formed by bridging Cr ions with nitrogen-containing pyrazine, has been synthesized via post-synthetic reduction of preassembled Cr metal ions and pyrazine building blocks.[32] This material has attracted enormous attention owing to its versatile nanostructures and promising potential for future spintronics applications.[33] For instance, $Cr(pyz)_2$ can be constructed into a 2D magnetic metal-organic framework, which provides an experimentally feasible chemical strategy to increase the Curie temperature.[34] Furthermore, the spin-transport properties of van der Waals junctions based on $Cr(pyz)_2$ can be significantly modulated by the tunneling barrier and dipole at the molecule-electrode interface.[35] However, the spin-dependent thermoelectric properties of one-dimensional Cr-pyrazine metal-organic molecular heterojunctions have not yet been explored.

In this work, we investigate the spin-dependent Seebeck effect of $Cr(pyz)_4$-based heterojunctions using first-principles calculations,[36] focusing on the modulation of thermoelectric performance by the twist between pyrazine rings and graphene electrodes. We find that the twist cannot only regulate CSI to improve conductance, but also control DSI to achieve a high Seebeck coefficient. Meanwhile, the twist enhances phonon scattering, leading to a lower phonon thermal conductance. As a result, the thermoelectric performance of the system is significantly improved.

2. Computational Methods. It is well known that layered $Cr(pyz)_2$ has been successfully synthesized in recent experimental studies.[32] With the aid of advanced molecular fabrication techniques such as scanning tunneling microscopy, atomic force microscopy,[37] and mechanically controlled break junction technique,[38] it has become possible to extract the molecule $Cr(pyz)_4$ from the layered $Cr(pyz)_2$. Using single-molecule junction technology[39] and thermoelectric junction technologies,[40] it is promising to not only construct $Cr(pyz)_4$ into $Cr(pyz)_4$-based heterojunctions precisely control their geometrical configurations, but also accurately measure their conductance[41] and Seebeck coefficient. In particular, recent breakthroughs in thermal transport measurements in molecular structures[42,43] have removed the final obstacle to measuring the thermoelectric figure of merit ZT. These advanced experimental techniques provide the possibility for us of constructing $Cr(pyz)_4$-based organic molecular heterojunctions and perform spin- and charge-dependent thermoelectric measurements on such quantum structures.

In this work, we characterize the structural models of the calculated molecular devices, as shown in Fig. 1. The first geometrical model is presented in Figs. 1(a1)–1(c1). Here, zigzag graphene nanoribbons (ZGNR) [M-ZGNR, where M is the number of carbon dimer lines across the ribbon width ($M = 6$ in this work)] are used for both the left and right electrodes, with the $Cr(pyz)_4$ molecule sandwiched between them. In this geometrical model, one Cr atom is four-coordinated with four pyrazine molecules in a planar configuration. The four pyrazine molecules arranged along the diagonal directions are initially tilted antiphase by 47.5°, and all four pyrazine molecules exhibit a clockwise tilting pattern. This structure is consistent with previous studies[34,35] and is named as $Cr(pyz)_4$@ZGNR-47.5°. Subsequently, we design another geometrical model by tuning the twist angle between the pyrazine rings and ZGNR, as illustrated in Figs. 1(a2)–1(c2). In this structure, one set of pyrazine molecules along the diagonal is initially oriented parallel to the electrodes, while the other set is oriented perpendicular to the electrodes. For convenience, this configuration is named $Cr(pyz)_4$@ZGNR-90°. It is well established that the spin direction of ZGNR electrodes can be controlled via an external magnetic field, and the spin state of the calculated molecular devices can be set to parallel (P) or antiparallel (AP).[44] Similarly, the four configurations under the two spin states are named as P-$Cr(pyz)_4$@ZGNR-47.5°, AP-$Cr(pyz)_4$@ZGNR-47.5°, P-$Cr(pyz)_4$@ZGNR-90°, and AP-$Cr(pyz)_4$@ZGNR-90°, respectively.

In our calculations, all geometric optimizations and electron and phonon transport calculations are performed using density-functional theory combined with the Keldysh non-equilibrium Green's function technique, which is implemented in the Atomistix ToolKit package (ATK).[45,46] For the exchange-correlation energy functional, the Perdew-Burke-Ernzerhof (PBE) version of the spin-dependent generalized gradient approximation (GGA) is employed. The residual force components of all atoms are less than 0.03 eV/Å, and a mesh cut-off energy of 200 Ry is chosen to achieve a balance between calculation efficiency and accuracy. As the macromolecular device contains more than 190 atoms, the energy tolerance for self-consistency is set to 10^{-3} eV during total energy and transport calculations. A double-zeta polarized basis set is selected for the electron wavefunction. A Monkhorst-Pack $1 \times 1 \times 50$ k-point grid is used for k-point sampling. The vacuum thickness along the two non-transport directions is set to greater than 15 Å to avoid interactions between periodic images. After optimizing the geometric structures, we obtain the spin-dependent electronic transmission function $\tau_\sigma(E)$ ($\sigma = \uparrow$ or $\downarrow$ denotes the spin index), and phonon transmission function $\tau_{\rm ph}(\omega)$. Then, the spin-dependent electron conductance, electron thermal conductance, and Seebeck coefficient can be calculated using the following equations:

$$G_\sigma(\mu) = e^2 \Gamma_\sigma^{(0)}(\mu, T), \tag{1}$$

$$K_{e,\sigma}(\mu, T) = \frac{1}{T}\left[\Gamma_\sigma^{(2)(\mu,T)} - \frac{(\Gamma_\sigma^{(1)})^2(\mu, T)}{\Gamma_\sigma^{(0)}(\mu, T)}\right], \tag{2}$$

$$S_\sigma(\mu, T) = \frac{1}{eT}\frac{\Gamma_\sigma^{(1)}(\mu, T)}{\Gamma_\sigma^{(0)}(\mu, T)}, \tag{3}$$

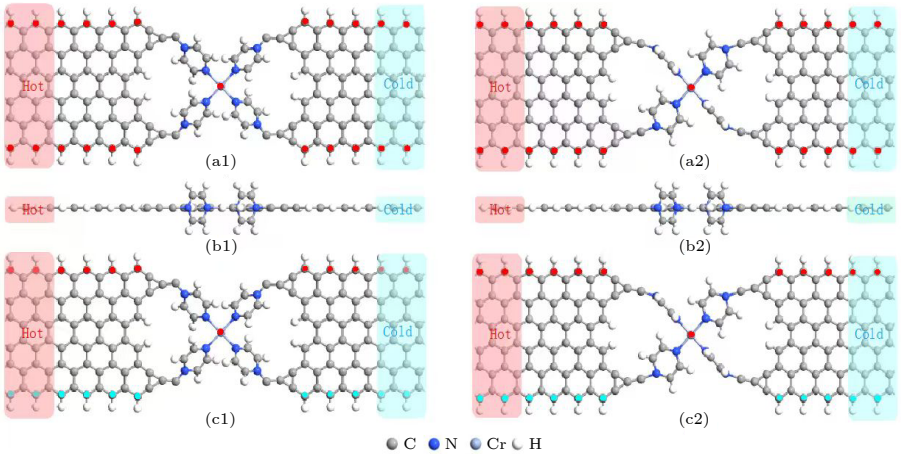

Fig. 1. Schematic of two types of configurations $Cr(pyz)_4$@ZGNR-47.5° in (a1)–(c1) and $Cr(pyz)_4$@ZGNR-90° in (a2)–(c2). The vertical views of [(a1) and (c1)] $Cr(pyz)_4$@ZGNR-47.5° and [(a2) and (c2)] $Cr(pyz)_4$@ZGNR-90°. The side views of (b1) $Cr(pyz)_4$@ZGNR-47.5° and (b2) $Cr(pyz)_4$@ZGNR-90°. The spin-magnetization density distribution for [(a1) and (a2)] P and [(c1) and (c2)] AP spin states, in which the red and cyan colors denote the up- and down-spin.

where $\Gamma_\sigma^{(m)}$ is an intermediate function, which can be expressed as [47]

$$\Gamma_\sigma^{(m)} = \frac{2}{h}\int_{-\infty}^{\infty}(E-\mu)^m\Big[-\frac{\partial f(E,\mu,T)}{\partial E}\Big]\tau_\sigma(E)\mathrm{d}E, \quad (4)$$

and $f(E,\mu,T)$ is a Fermi-Dirac distribution function, h is the Planck constant, μ is chemical potential, and E is the energy of electron. The phonon thermal conductance can be expressed as [48]

$$K_{\mathrm{ph}} = \frac{\hbar^2}{k_{\mathrm{B}}T^2}\frac{1}{2\pi}\int_0^{\infty}\tau(\omega)\frac{\omega^2 \mathrm{e}^{\beta\hbar\omega}}{(\mathrm{e}^{\beta\hbar\omega}-1)^2}\mathrm{d}\omega. \quad (5)$$

Then, the spin-dependent (charge-dependent) figure of merit $Z_{\mathrm{sp(ch)}}T$ is calculated by the standard expression:

$$Z_{\mathrm{sp(ch)}}T = TG_{\mathrm{sp(ch)}}S_{\mathrm{sp(ch)}}^2/(K_{\mathrm{e}}+K_{\mathrm{ph}}), \quad (6)$$

where G_σ (S_σ) indicates the conductance (Seebeck coefficient) of a given channel σ; $S_{\mathrm{sp}} = S_\uparrow - S_\downarrow$ [$S_{\mathrm{ch}} = (S_\uparrow + S_\downarrow)/2$] is the spin-dependent (charge-dependent) Seebeck coefficient; and $G_{\mathrm{sp}} = |G_\uparrow - G_\downarrow|$ ($G_{\mathrm{ch}} = G_\uparrow + G_\downarrow$) is the spin-dependent (charge-dependent) electrical conductance, [49] respectively. In this study, we neglect the effect of electron-phonon coupling on the thermoelectric performance because the size of the studied system is smaller than the inelastic mean free path of phonons, resulting in ballistic transport for both electron and phonon transport. [50]

3. Results and discussion. To evaluate the regulatory effect of the twist between the pyrazine ring planes and ZGNR on the thermoelectric conversion performance, we calculate the spin ZT value $Z_{\mathrm{sp}}T$ and charge ZT value $Z_{\mathrm{ch}}T$ of $Cr(pyz)_4$@ZGNR-47.5° and $Cr(pyz)_4$@ZGNR-90°, as shown in Fig. 2. As shown in Fig. 2(a) for the P spin quantum structure calculated, the $Z_{\mathrm{sp}}T$ of P-$Cr(pyz)_4$@ZGNR-90° at $\mu = 0.93$ eV can exceed 4 at room temperature and reach 6 at 340 K. This value is comparable to the results in twisted triangulene π-dimer junctions [24] and much higher than those reported in spin semiconducting armchair graphene nanoribbons. [49] In contrast, the peak $Z_{\mathrm{sp}}T$ of P-$Cr(pyz)_4$@ZGNR-47.5° is much lower than that of P-$Cr(pyz)_4$@ZGNR-90°, being only 0.29 at 340 K and 0.34 at 300 K. A significant twist-induced enhancement in $Z_{\mathrm{ch}}T$ is also observed in Fig. 2(b). For instance, the $Z_{\mathrm{ch}}T$ of $Cr(pyz)_4$@ZGNR-90° can reach 0.64 at 340 K and 0.61 at 300 K, nearly twice that of P-$Cr(pyz)_4$@ZGNR-47.5°. For the AP spin state, although its ZT peaks are much lower than those of the P spin state, such twist-induced ZT enhancement can still be observed in Figs. 2(c) and 2(d). For example, the peak $Z_{\mathrm{sp}}T$ of AP-$Cr(pyz)_4$@ZGNR-90° reaches 0.5 at 300 K and 0.49 at 340 K, while the peaks of AP-$Cr(pyz)_4$@ZGNR-47.5° are all below 0.2 for temperatures $T \leq 340$ K. In addition, it can be clearly seen from Fig. 2(d) that the peak $Z_{\mathrm{ch}}T$ of AP-$Cr(pyz)_4$@ZGNR-90° is also enhanced compared with that of AP-$Cr(pyz)_4$@ZGNR-47.5°. These results demonstrate that the observed enhancements in thermoelectric performance are entirely attributed to the twist effect between the pyrazine rings and ZGNR.

To elucidate the reason for the twist-induced thermoelectric enhancement, we present in Fig. 3 the spin-resolved transmission spectra under P and AP spin states. For the spin-up transmission spectra, regardless of the P or AP spin state, although the overall transmission spectra of $Cr(pyz)_4$@ZGNR-47.5° and $Cr(pyz)_4$@ZGNR-90° are rather similar, the transmission coefficients of $Cr(pyz)_4$@ZGNR-90° are much larger than those of $Cr(pyz)_4$@ZGNR-47.5° within the energy range from −1.3 to 0.8 eV. In particular, numerous transmission peaks contributed by CSI can be observed in $Cr(pyz)_4$@ZGNR-90°. To interpret these results, we calculate the SPLDOS, as shown in Figs. 3(c) and 3(d). Clearly, the spin-up electronic states of $Cr(pyz)_4$@ZGNR-90° are distributed more uniformly than those of $Cr(pyz)_4$@ZGNR-47.5° within the coupling region of the device, which facilitates electron tunneling through the former and thus leads to a higher transmission coefficient. Especially near 0.8 eV, −0.3 eV, and −1.3 eV, electrons in $Cr(pyz)_4$@ZGNR-90° exhibit a uniform alternating pattern of magenta and blue spin density distributions across the entire real space, showing

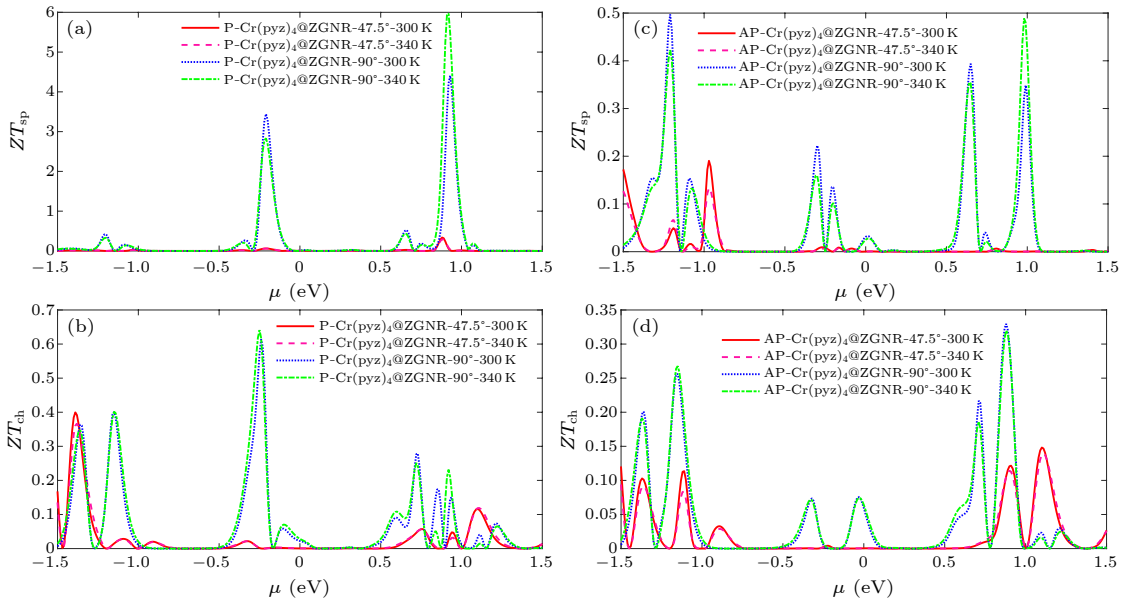

Fig. 2. (a) $Z_{\rm sp}T$ and (b) $Z_{\rm ch}T$ as a function of the chemical potential μ for P spin state at different temperatures. (c) $Z_{\rm sp}T$ and (d) $Z_{\rm ch}T$ as a function of the chemical potential μ for AP spin state at different temperatures.

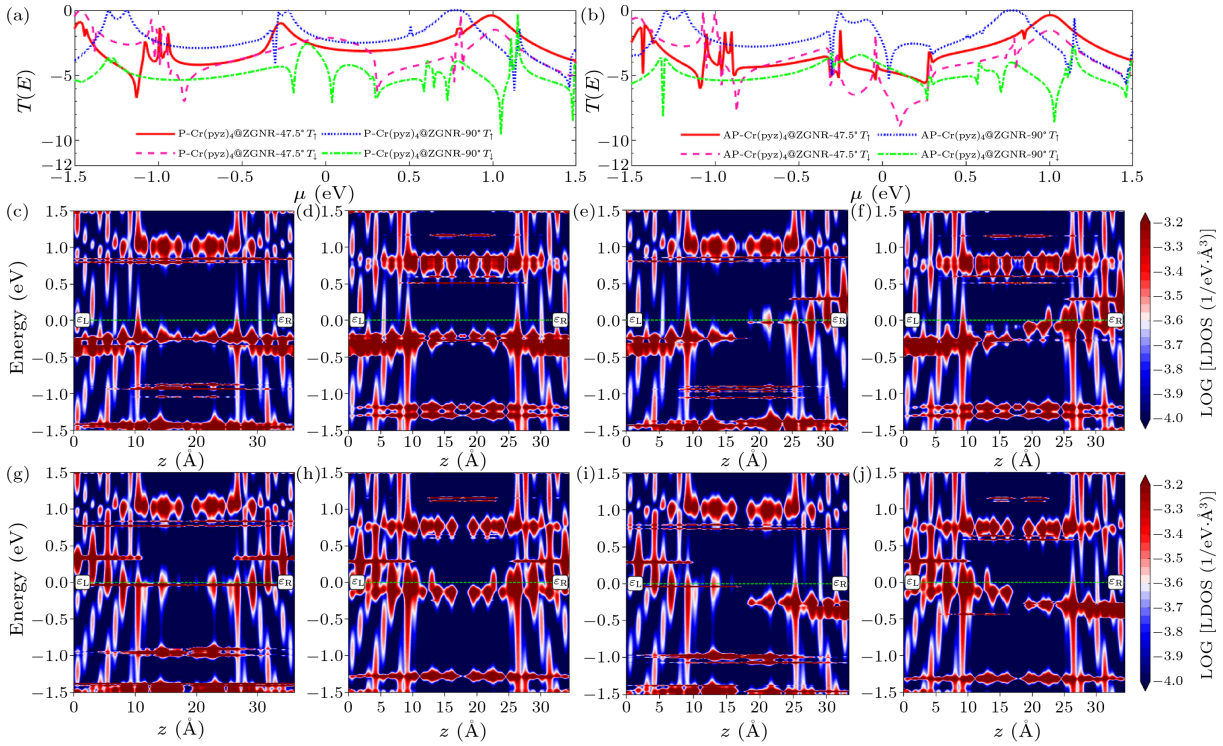

Fig. 3. (a) P and (b) AP transmission spectra of the up- and down-spin, respectively. (c) and (d) Up-spin spatially-resolved projected local density of states (SPLDOS) for $Cr(pyz)_4$@ZGNR-47.5° and $Cr(pyz)_4$@ZGNR-90° in the P spin state. (g) and (h) Down-spin SPLDOS for $Cr(pyz)_4$@ZGNR-47.5° and $Cr(pyz)_4$@ZGNR-90° in the P spin state. (e) and (f) Up-spin SPLDOS for $Cr(pyz)_4$@ZGNR-47.5° and $Cr(pyz)_4$@ZGNR-90° in the AP spin state. (i) and (j) Down-spin SPLDOS for $Cr(pyz)_4$@ZGNR-47.5° and $Cr(pyz)_4$@ZGNR-90° in the AP spin state. The magenta and blue colors represent the distribution regions of the high and low densities of states, respectively.

clear signatures of CSI. Further calculations reveal that the SPLDOS of $Cr(pyz)_4$@ZGNR-47.5° at around −1.15 eV is extremely low in the central region. As a result, the spin-up state exhibits not only an extremely low transmission coefficient but also an antiresonant DSI. After twisting the geometric configuration of the central region, we find that the spin-up SPLDOS at this energy position in structure $Cr(pyz)_4$@ZGNR-90° becomes more uniform and higher in both the central and coupling regions. This reverses the transmission interference pattern at this energy level: the spin-up state shows not only a very high transmission coefficient but also distinct resonant CSI. For the spin-down transmission spectra, regardless of the P or AP spin state, the SPLDOS in the central region of $Cr(pyz)_4$@ZGNR-47.5° is extremely low within the calculated energy range. This leads to not only very low transmission coefficients

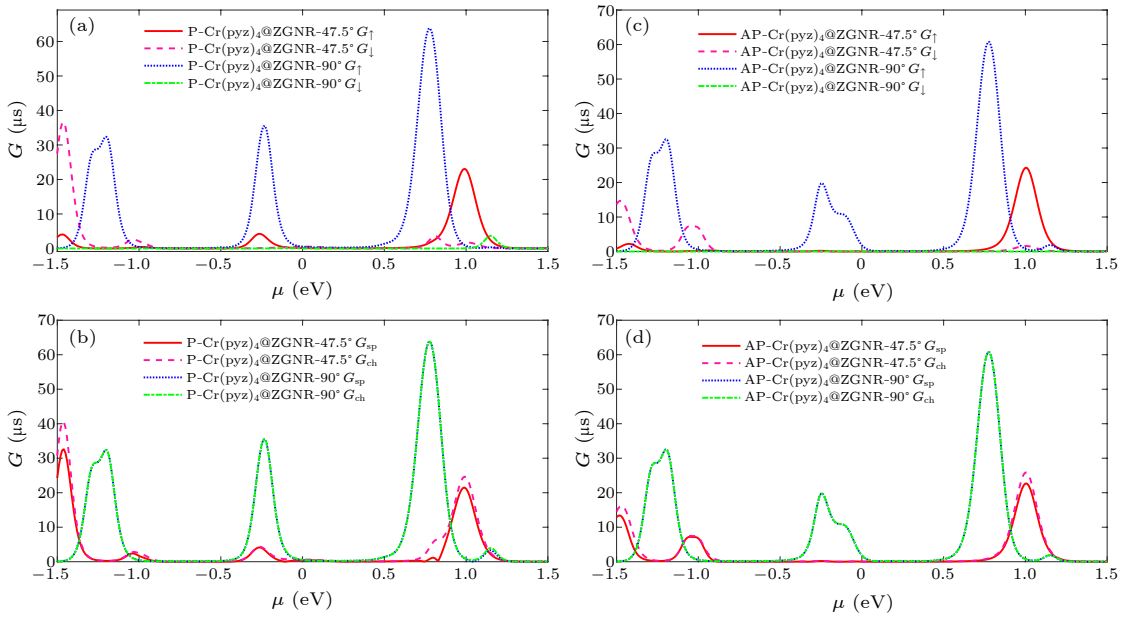

Fig. 4. (a) Up- and down-spin electronic conductances, (b) spin- and charge-dependent conductances in the P spin state, (c) up- and down-spin electronic conductances, (d) spin- and charge-dependent conductances in the AP spin state show the dependence on the chemical potential μ at $T = 300\,\mathrm{K}$.

Table 1. Comparison of room temperature thermoelectric properties, σ (μS), κ_e (pW/K), κ_{ph} (pW/K), S (μV/K) and ZT values with other junctions.

Structure	σ	κ_e	κ_{ph}	S	ZT	$E - E_F$
P-Cr(pyz)$_4$@ZGNR-90° (our work)	5.5	39.4	164.7	737	4.4	0.93
Zig-NH-G [54]	11	37	398	−425	0.5	−0.51
PL_9 [24]	11.6	49.1	255	−178	0.4	0.6
Triangulene π-dimer junctions [53]	53	300	9.7	470	5.3	0
Boron-stabilized triphenylmethyl (TPM-B) [10]	$7.75 \times 10^{-3} \sim 1.23$	–	–	–	–	0
Ppy-M1 junction [20]	28.6	55	33.6	776.3	36.5	−0.1
Si2-Si222-Si2 [2]	–	–	–	970	–	Exp.
Single-alkanedithiol junctions [42]	–	–	20	–	–	Exp.
Phenothiazine dihydrobenzo[b]thiophene [51]	$7.75 \times 10^{-5} \sim 38.84$	–	–	–	–	Exp.
Dihydrobenzo thiophene-OPE3 [43]	0.014	0.46	23.5	−8.7	–	Exp.

but also several antiresonant DSIs. After twisting the geometry of the central region, we find that the SPLDOS in the central region of Cr(pyz)$_4$@ZGNR-90° becomes more inhomogeneous and even lower, resulting in smaller electronic transmission coefficients and sharper antiresonant DSIs. This means that the DSI is very sensitive to the dihedral angle between the ZGNR and the neighboring pyrazine molecules, a phenomenon that is also similar to previous studies. [30] Notably, the deepest transmission antiresonance $\simeq 10^{-10}$ caused by DSI appears at 1.2 eV, which can provide a strong advantage for the highest Seebeck coefficient S discussed later.

We next discuss the effect of structural twist on the electronic conductance. As can be seen from Fig. 4, under both P and AP spin states, the $G_\uparrow$ values of Cr(pyz)$_4$@ZGNR-90° are much larger than those of Cr(pyz)$_4$@ZGNR-47.5°, which is particularly evident near the three equally spaced conductance peaks at the chemical potentials $\mu = 0.8\,\mathrm{eV}$, $-0.3\,\mathrm{eV}$, and $-1.3\,\mathrm{eV}$. This arises because the transmission coefficient $\tau_\uparrow(E)$ exhibits high transmission peaks contributed by CSI at these energies. The transmission peaks of spin-up electrons lead to a pronounced enhancement in conductance, which is consistent with the trends in other theoretical studies [10,20] and experimental measurements, [51] (see Table 1). Meanwhile, owing to the very low spin-down transmission coefficients, the spin-down conductance $G_\downarrow$ of both quantum systems is much smaller than the spin-up conductance. Therefore, as shown in Figs. 4(b) and 4(d), the spin conductance $G_{sp} = |G_\uparrow - G_\downarrow| \simeq G_\uparrow$ and the charge conductance $G_{ch} = G_\uparrow + G_\downarrow \simeq G_\uparrow$. The conductance of the system is determined collectively by the transmission coefficients of spin-up and spin-down electrons. Upon structural twisting, in both P and AP spin configurations, the increase in the spin-up transmission coefficient for Cr(pyz)$_4$@ZGNR-90° is far greater than the decrease in the spin-down transmission coefficient, resulting in a significant enhancement of the system's total transmission coefficient. Such variations in the electronic transmission coefficients give rise to a remarkable improvement in both G_{sp} and G_{ch} for Cr(pyz)$_4$@ZGNR-90°, which is one of the main reasons why the maximum dependent figure of merit $Z_{sp}T_{Max}$ and maximum dependent figure of merit $Z_{ch}T_{Max}$ for Cr(pyz)$_4$@ZGNR-90° are substantially larger than those for Cr(pyz)$_4$@ZGNR-47.5°.

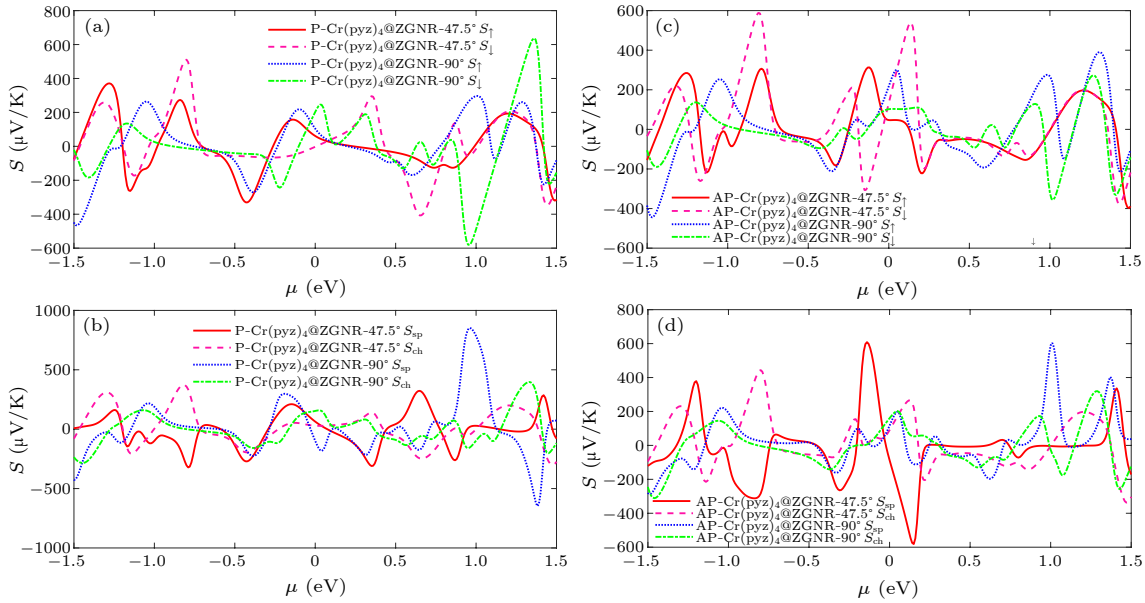

Fig. 5. The dependence on the chemical potential μ at $T = 300$ K is shown for (a) up- and down-spin Seebeck coefficients in the P spin state, (b) spin- and charge-dependent Seebeck coefficients in the P spin state, (c) up- and down-spin Seebeck coefficients in the AP spin state, and (d) spin- and charge-dependent Seebeck coefficients in the AP spin state.

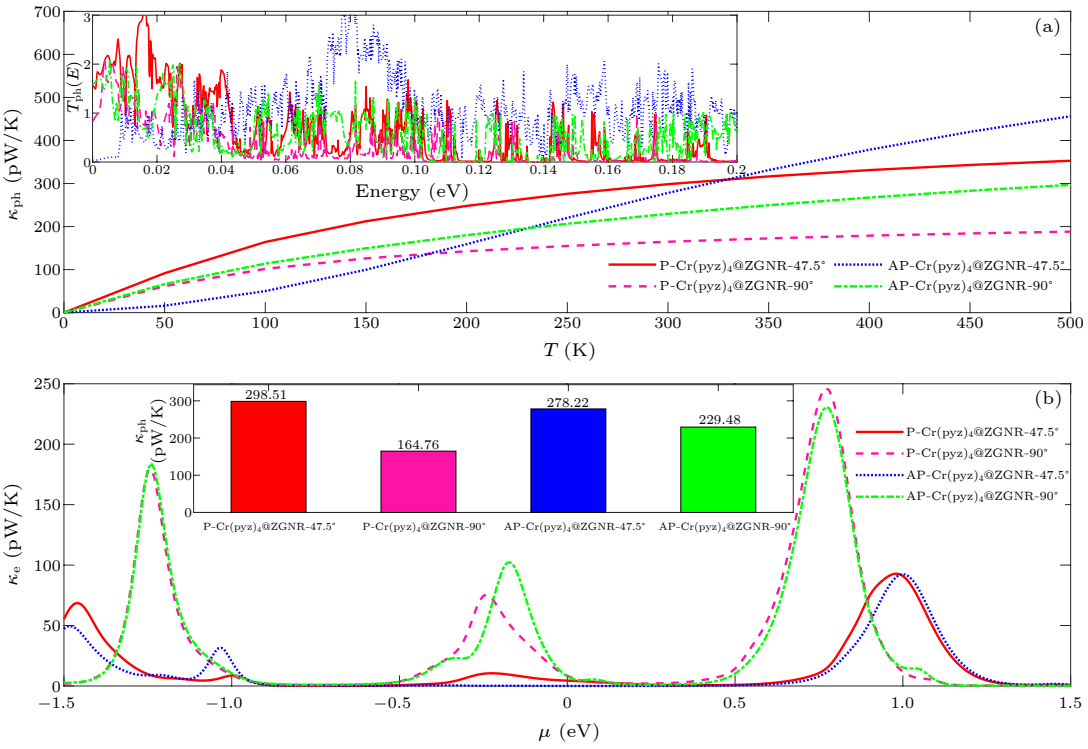

Fig. 6. (a) The phonon thermal conductance is shown as a function of temperature for different configurations or spin states. (b) The electrical thermal conductance is shown as a function of chemical potential μ at $T = 300$ K for different configurations or spin states. The insets in (a) and (b) describe the corresponding phonon transmission function and the phonon thermal conductance at temperature $T = 300$ K, respectively.

We also investigate the effect of twisting on the Seebeck coefficient, and the results are shown in Fig. 5. Obviously, for the P spin state in Fig. 5(a), both $S_\uparrow$ and $S_\downarrow$ exhibit multiple peaks, which mainly originate from the resonant and antiresonant effects of electron transport $[S(T,\psi) \approx \frac{\pi^2 k_B^2 T}{3e} \frac{\partial \ln T_e}{\partial E}|_\mu$ [52]]. It can be clearly seen that the peak values of $S_\downarrow$ are significantly larger than those of $S_\uparrow$, which is mainly attributed to the extremely sharp transmission antiresonance induced by DSI. For instance, near the chemical potential $\mu = 1$ eV, negative $S_\downarrow$ is observed in Cr(pyz)$_4$@ZGNR-90°, with a maximum absolute value up to 600 μV/K. This arises from the extremely sharp transport antiresonance caused by DSI at this chemical potential in Cr(pyz)$_4$@ZGNR-90° [see Fig. 3(a)]. In addition, within the energy range 0.8–1.1 eV, Cr(pyz)$_4$@ZGNR-90° also shows positive $S_\uparrow$ with a peak

value up to 300 μV/K. Consequently, the spin-resolved Seebeck coefficient S_{sp} can reach as high as 850 μV/K at $\mu = 1.0$ eV, which is consistent with the trends of other theoretical studies[20] and experimental measurements[51] (see Table 1). This is another important reason for the extremely high peak value of $Z_{sp}T$ in Cr(pyz)$_4$@ZGNR-90°. Furthermore, Cr(pyz)$_4$@ZGNR-47.5° exhibits an extremely deep transport antiresonance induced by DSI at $E = -0.8$ eV [see Fig. 3(a)], leading to an extremely high positive peak of $S_\downarrow$. However, a positive peak of $S_\uparrow$ also exists at this energy. Given $S_{sp} = S_\uparrow - S_\downarrow$, the magnitude of S_{sp} for this quantum configuration is not very large [see Fig. 5(b)]. For the AP spin state, multiple similar high $S_\downarrow$ peaks appear in both quantum geometries due to DSI [see Fig. 5(c)]. At many $S_\downarrow$ peak positions, several $S_\uparrow$ peaks with opposite signs are simultaneously present. These factors together not only produce a high S_{sp} but also make the S_{sp} peak larger than the charge Seebeck coefficient S_{ch} peak [see Fig. 5(d)]. Combined with the previous findings, we find that twisting can lead to a substantial increase in both the conductance and the Seebeck coefficient in the P and AP spin states. Particularly interestingly, in the P spin state, the peak positions of conductance almost perfectly coincide with those of the Seebeck coefficient, which is the fundamental reason for the relatively high ZT value achieved in the twisted structure Cr(pyz)$_4$@ZGNR-90°. In contrast, in the AP spin state, the conductance peaks and Seebeck coefficient peaks are clearly separated, resulting in a much lower ZT value in the twisted structure Cr(pyz)$_4$@ZGNR-90° than that under the P spin state.

Finally, we investigate the dependence of thermal transport properties on geometric configuration and spin type. For the P spin state, the scattering strength in P-Cr(pyz)$_4$@ZGNR-90° is much stronger than that in P-Cr(pyz)$_4$@ZGNR-47.5° in both the low-energy and high-energy regions. This results in much lower phonon transmission coefficients and phonon thermal conductances in P-Cr(pyz)$_4$@ZGNR-90° than in P-Cr(pyz)$_4$@ZGNR-47.5° from low to high temperatures. In contrast, for the AP spin state, the scattering strength in AP-Cr(pyz)$_4$@ZGNR-47.5° is much stronger than that in AP-Cr(pyz)$_4$@ZGNR-90° in the low-energy region 0–0.03 eV. Therefore, the thermal conductance of AP-Cr(pyz)$_4$@ZGNR-47.5° is lower than that of AP-Cr(pyz)$_4$@ZGNR-90° in the temperature range $0\,\text{K} < T < 230\,\text{K}$. When the temperature further rises above 230 K, high-frequency phonons are excited, and the scattering strength of the two structures is reversed, which leads to larger phonon transmission coefficients and phonon thermal conductances in AP-Cr(pyz)$_4$@ZGNR-47.5° at high temperatures. The calculated thermal conductance values are also of the same order of magnitude as those in previous theoretical calculations[53,54] (see Table 1). Figure 6 also presents the variation of the electronic thermal conductance K_e as a function of the chemical potential μ at room temperature. The results show that K_e exhibits a similar trend to G_{ch}: the K_e of P-Cr(pyz)$_4$@ZGNR-90° $\simeq$ K_e of AP-Cr(pyz)$_4$@ZGNR-90° $>$ K_e of P-Cr(pyz)$_4$@ZGNR-47.5° $\simeq$ K_e of AP-Cr(pyz)$_4$@ZGNR-47.5°. At temperature $T = 300$ K, compared with the phonon thermal conductance K_{ph}, the electronic thermal conductance K_e of Cr(pyz)$_4$@ZGNR-47.5° in both P and AP spin states is significantly lower, indicating that phonon thermal conductance dominates the total thermal conductance in this structure. Notably, the K_{ph} of P- and AP-Cr(pyz)$_4$@ZGNR-90° is significantly lower than that of P- and AP-Cr(pyz)$_4$@ZGNR-47.5° for both the P-spin and AP-spin states, which is another reason why the peak values of $Z_{sp}T$ and $Z_{ch}T$ for P- and AP-Cr(pyz)$_4$@ZGNR-90° are higher than those for P- and AP-Cr(pyz)$_4$@ZGNR-47.5°.

4. Conclusion. In summary, based on density functional theory combined with the non-equilibrium Green's function method, we systematically investigate the spin-dependent thermoelectric properties of the Cr(pyz)$_4$ (pyz = pyrazine) magnetic molecule coupled to two ferromagnetic ZGNR electrodes by varying the twisting angle between the pyrazine ring planes and the ZGNR electrodes. The results show that adjusting the twisting angle can significantly improve the thermoelectric performance. Such an enhancement in thermoelectric performance can be mainly attributed to the following three aspects: (i) twisting induces CSI, thereby increasing the spin-dependent electronic conductance; (ii) twisting gives rise to transmission antiresonances caused by DSI, which can greatly enhance the spin Seebeck coefficient; (iii) twisting strengthens phonon scattering, leading to an extremely low phonon thermal conductance. Our study demonstrates that twisting is a highly effective degree of freedom for effectively regulating and enhancing the thermoelectric properties of molecular thermoelectric devices.

Acknowledgements. This work was supported by the Hunan Provincial Natural Science Foundation of China (Grant No. 2026JJ80847), the Hunan Provincial Natural Science Foundation Regional Joint Fund Project (Grant No. 2025JJ70508), the College Student Innovation Training Fund (Grant No. 202510538040), the key projects of Hunan Provincial Department of Education (Grant No. 21A0167), and the Talent Introducing Foundation of Central South University of Forestry and Technology (Grant No. 104-0160).

References

[1] Bai J, Daaoub A, Sangtarash S *et al.* 2019 *Nat. Mater.* **18** 364
[2] Garner M H, Li H X, Chen Y *et al.* 2018 *Nature* **558** 415
[3] Huang L, Zhou Y, Chen Y, Ye J, Liu J, Xiao Z, Tang C, Xia H, and Hong W 2021 *Sci. China Mater.* **64** 1426
[4] Bergfield J P 2024 *Nano Lett.* **24** 15110
[5] Ma L, Nian L L, and Lv J T 2020 *Phys. Rev. B* **101** 045410
[6] Bennett R X, Hendrickson J R, and Bergfield J P 2024 *ACS Nano* **18** 11876
[7] Bai S, Zhang X, and Zhao L D 2023 *Acc. Chem. Res.* **56** 3065
[8] Chen Z X, Deng J R, Hou S J *et al.* 2023 *J. Am. Chem. Soc.* **145** 15265
[9] Chen H, Chen Y R, Zhang H W *et al.* 2022 *Chin. Chem. Lett.* **33** 523

[10] Chelli Y, Sandhu S, Daaoub A H S, Sangtarash S, and Sadeghi H 2023 *Nano Lett.* **23** 3748
[11] Zhang L, Tan S H, Peng X F, and Long M Q 2025 *Chin. Phys. Lett.* **42** 066601
[12] Chen W Y, Shi X L, Zou J, and Chen Z G 2022 *Small Methods* **6** 2101235
[13] Neophytou N, Vargiamidis V, Foster S, Graziosi P, de Sousa Oliveira L, Chakraborty D, and Narducci D 2020 *Eur. Phys. J. B* **93** 213
[14] Zhou C J, Lee Y K, Yu Y Z *et al.* 2021 *Nat. Mater.* **20** 1378
[15] Jia P Z, Deng L Q, Deng X G, Wang B K, Yu X, Chen X K, Wu D, Xie Z X, and Zhou W X 2025 *Appl. Phys. Lett.* **127** 193102
[16] Hu L, Wu H, Zhu T, Fu C, He J, Ying P, and Zhao X 2015 *Adv. Energy Mater.* **5** 1500411
[17] Xiao Y, Wu H, Li W, Yin M, Pei Y, Zhang Y, and Zhao L D 2017 *J. Am. Chem. Soc.* **139** 18732
[18] Xiao Y, Wang D, Qin B, Wang J, Wang G, and Zhao L D 2018 *J. Am. Chem. Soc.* **140** 13097
[19] Yang H, Ding C, Duan Z, Zeng J, Tang L M, Luo N, and Chen K Q 2025 *Appl. Phys. Lett.* **126** 202202
[20] Huang L, Wang J, Chen T, Xu L, Ning F, Wu D, and Chen K Q 2024 *Appl. Phys. Lett.* **124** 102403
[21] Zhang P P, Tan S H, Long M Q, and Peng X F 2019 *Appl. Phys. Express* **12** 125005
[22] Ojeda J H, Maiti S K, Laroze D, Eramo G, and Orellana P A 2025 *J. Chem. Phys.* **162** 244115
[23] Li J, Wang B, Xu F, Wei Y, and Wang J 2016 *Phys. Rev. B* **93** 195426
[24] Wu D, Huang L, Jia P Z, Cao X H, Fan Z Q, Zhou W X, and Chen K Q 2021 *Appl. Phys. Lett.* **119** 063503
[25] Wu D, Cao X H, Chen S Z, Tang L M, Feng Y X, Chen K Q, and Zhou W X 2019 *J. Mater. Chem. A* **7** 19037
[26] Alsaqer M, Daaoub A H S, Sangtarash S, and Sadeghi H 2023 *Nano Lett.* **23** 10719
[27] Markussen T, Stadler R, and Thygesen K S 2010 *Nano Lett.* **10** 4260
[28] Miao R, Xu H, Skripnik M *et al.* 2018 *Nano Lett.* **18** 5666
[29] Yan S, Luan Y X, Xu H L 2024 *Nanoscale* **16** 13905
[30] Almughathawi R, Hou S, Wu Q, Liu Z, Hong W, and Lambert C 2021 *ACS Sens.* **6** 470
[31] Hurtado-Gallego J, Sangtarash S, Davidson R *et al.* 2022 *Nano Lett.* **22** 948
[32] Perlepe P, Oyarzabal I, Mailman A *et al.* 2020 *Science* **370** 587
[33] Feng Q, Li X, and Li X 2024 *Nano Lett.* **24** 3462
[34] Lv H, Li X, Wu D, Liu Y, Li X, Wu X, and Yang J 2022 *Nano Lett.* **22** 1573
[35] Ge M, Liu Z, Chen T, Xu L, and Huang L 2025 *Phys. Chem. Chem. Phys.* **27** 6255
[36] Ding C H, Liu W, Yao Y, Chen H, Luo N, Zeng J, Tang L M, Pan H, and Chen K Q 2026 *Phys. Rev. B* **113** 115403
[37] Ferreira Q, Braganca A M, Alcácer L, and Morgado J 2014 *J. Phys. Chem. C* **118** 7229
[38] Li Q and Solomon G C 2014 *Faraday Discuss.* **174** 21
[39] Xie X M, Li P H, Xu Y X, Zhou L, and Yan Y 2022 *ACS Nano* **16** 3476
[40] He P, Jang J, Kang H G, and Yoon H J 2025 *Chem. Rev.* **125** 2953
[41] Zeng Y J, Wu D, Cao X H, Zhou W X, Tang L M, and Chen K Q 2019 *Adv. Funct. Mater.* **30** 1903873
[42] Cui L, Hur S, Akbar Z A *et al.* 2019 *Nature* **572** 628
[43] Gemma A, Tabatabaei F, Drechsler U *et al.* 2023 *Nat. Commun.* **14** 3868
[44] Wu Q H, Zhao P, Liu D S, Li S J, and Chen G 2014 *Organic Electron.* **15** 3615
[45] Taylor J, Guo H, and Wang J 2001 *Phys. Rev. B* **63** 245407
[46] Liu Q, Zhen Z, Xie H Q, Fan Z Q, Wu D, and Chen K Q 2025 *Appl. Phys. Lett.* **127** 092104
[47] Jiang J W, Wang J S, and Li B 2011 *J. Appl. Phys.* **109** 014326
[48] Peng X F, Chen K Q, Wan Q, and Zou B S 2010 *Phys. Rev. B* **81** 195317
[49] Shirdel-Havar M and Farghadan R 2018 *Phys. Rev. B* **97** 235421
[50] Gan Y B, Liu X Y, Tang W S, Cao X H, Fan Z Q, and Wu D 2024 *J. Appl. Phys.* **136** 135101
[51] Liu J, Zhao X, Al-Galiby Q *et al.* 2017 *Angew. Chem. Int. Ed.* **56** 13061
[52] Guttman G D, Ben-Jacob E, and Bergman D J 1995 *Phys. Rev. B* **51** 17758
[53] Wu D, Cao X H, Jia P Z, Zeng Y J, Feng Y X, Tang L M, and Chen K Q 2020 *Sci. China Phys. Mech. Astron.* **63** 276811
[54] Yu X, Liu J H, Zhou W X *et al.* 2023 *Phys. Chem. Chem. Phys.* **25** 19082